*Journal of Applied Fluid Mechanics*, Vol. 17, No. 2, pp. 424-441, 2024.
Available online at www.jafmonline.net, ISSN 1735-3572, EISSN 1735-3645.
https://doi.org/10.47176/jafm.17.02.2069

# Erosion Wear Characteristics and Failure Mechanism of the Sulzer Oil Pump

L. F. Qiao[1], L. Mo[1], L. J. Mao[2†], J. L. Zhu[3], and L. X. Zeng[4]

[1] *School of mechanical engineering, Southwest Petroleum University, Sichuan, Chengdu, 610500, China*
[2] *State Key Laboratory of Oil and Gas Reservoir Geology and Exploitation, Southwest Petroleum University, Sichuan, Chengdu, 610500, China*
[3] *CNOOC Research Institute Ltd. Beijing, 100028, China*
[4] *Downhole Service Company, CNPC Chuanqing Drilling Engineering Co., Ltd. Chengdu, Sichuan 610213, China*

*†Correspondence Author E-mail: maoliangjie@qq.com*

## ABSTRACT

In the routine maintenance of each main pump in the oil transmission station plant, abnormal erosion wear was found at the flushing port of the mechanical seal of Sulzer pump casing. For the sake of stable and safe unit operation, this study explored the mechanism and process of erosion formation in the pump casing at the microscopic level using SEM (scanning electron microscope) and EDS (energy dispersive spectrometer) techniques. And ANSYS Fluent was used to numerically simulate the unconventional turbulent flow in the special location of Sulzer pump to obtain its flow field characteristics. The trajectory tracking of solid phase particles based on Finnie erosion model was also carried out to obtain the influence law of different particle sizes on the wear degree of each area of the pump casing, and to point out the influence of the motion behavior of particles at the flushing port position on the erosion. The results show that there is unconventional turbulence in the flushing port of the Sulzer pump mechanical seal, and the solid particles are affected by turbulent diffusion and fluid adhesion, and some particles deviate from the velocity direction and continuously impact the surface of the pump casing, which is the direct cause of the erosion wear here. By optimizing the location of the flushing port, severe erosion wear at the flushing port can be avoided. This study can provide guidance and recommendations for the production, operational stability and wear protection of Sulzer pumps.

***Article History***

*Received June 9, 2023*
*Revised August 24, 2023*
*Accepted September 28, 2023*
*Available online December 4, 2023*

***Keywords:***

*Erosion*
*Centrifugal Pump*
*EDS*
*SEM*
*Failure Mechanism*

## 1. INTRODUCTION

The Sulzer pump is the core equipment for transporting refined oil products during oil and gas development and stimulation (Fig. 1). Its working condition and life directly affect the efficiency and cost of oil and gas transportation. Given the complexity of the conveying medium in the pump and the inevitable existence of mechanical impurity particles, high-speed fluid and impurity particles will impact the surface of the internal flow channel at a certain speed and angle, resulting in serious erosion and wear (Fig. 2). In the long run, this result will affect the stability and safety of the oil transmission unit. Therefore, the erosion wear characteristics and the wear mechanism of the Sulzer pump must be studied to determine the causes of erosion. Erosion wear is a phenomenon in which some small and discrete particles that follow the flow of fluid wear or destroy the surface of an object when they collide with it, which is a common wear phenomenon in various industrial fields (Feller et al., 1984).

The Sulzer pump, the research object of this study, is a typical double-suction centrifugal pump with large flow delivery, compact structure, and high efficiency, which is widely used in the petrochemical industry. With the continuous progress of technology, more and more scholars choose to use the numerical simulation method to study the flow of fluid in the centrifugal pump and the erosion of particles on the outer wall.Material and fluid parameters can affect the erosion wear rate of turbomachinery, and related prediction models have also been proposed (Hattori & Kishimoto 2008). Shah & Jain (2008) pointed out that, in the hydraulic fracturing operation using coiled tubing, uneven erosion and wear of the tubing wall will occur. They conducted computational fluiddynamics (CFD) research, pointing out that the mud flow rate is the most important factor affecting erosion. Chandel et al. (2012) built an experimental platform to explore the impact of solid concentration and

**NOMENCLATURE**

| | | | |
|---|---|---|---|
| $a_k$ | volume fraction of the k-th term | $\sigma_f$ | flow stress |
| $\rho_k$ | density of the k phase | $h_c$ | depth of cut |
| $v_k$ | velocity of the k-th phase | K | drag coefficient |
| t | time | $\theta$ | impact angle of solid particles on target surface |
| p | pressure | $\varepsilon_N$ | ormal restitution coefficient |
| $\tau_k^{'}$ | molecular stress | $\varepsilon_T$ | tangential restitution coefficient |
| $\tau_k$ | turbulent stress | $v_{1,N}$ | normal velocity component of particle velocity before collision |
| $M_k$ | interphase momentum transfer per unit volume | $v_{1,\mathrm{T}}$ | tangential velocity component of particle velocity before collision |
| $(F_{\mathrm{int}})_k$ | intrinsic force | $v_{2,N}$ | normal velocity component of particle velocity after collision |
| g | acceleration of gravity | $v_{2,\mathrm{T}}$ | tangential velocity component of particle velocity after collision |
| $\rho_s$ | solid density | $\alpha$ | particle impact angle |
| $F_D$ | fluid flow around solid surfaces | $D$ | impeller outer diameter |
| $F_{other}$ | the sum of centrifugal force, Coriolis force, Basset force and Magnus lift | b | impeller outlet width |
| $W$ | volume loss due to wear and tear | $Z$ | number of blades |
| $m_p$ | the mass of solid particles | Q | rate of flow |
| $u_p$ | the velocity of a solid particle | H | head |
| n | rotate speed | $E$ | dimensionless erosion mass |
| $k$ | the model constant; | $V_p$ | particle impact velocity; |
| $f(\gamma)$ | Non-variable function of angle | | |

**Fig. 1 Appearance of the Sulzer oil delivery centrifugal pump**

rotation speed on the erosion wear of centrifugal pump and pointed out that the wear strongly depends on the size and rotation speed of solid particles. Walker & Robbie (2013) pointed out through experiments that the explanation for the different wear rates between the laboratory and field tests was postulated to be nonrepresentative wear mechanisms. This explanation is compounded by the lack of understanding of specific wear conditions in the pump (local velocity, concentration, particle size, size distribution, and particle shape) as well as the microstructure of the samples. Tarodiya & Gandhi (2017) proposed that the selection of pump materials, the properties of solid particles, the flow characteristics of fluids, and the concentration of solids play an important role in optimizing pump design. They proposed a method to predict the wear area based on numerical simulation. Through experimental research and numerical simulation, Zhang et al. (2016) evaluated the corrosion of fracturing pipelines under the action of multiphase flow and pointed out the damage mechanism of erosion wear and the main parameters of erosion impact factors. By introducing the Archard wear model, Huang et al. (2019) calculated the wear laws of the leading edge of the impeller blade, the blade tip, the blade pressure side, the blade suction side, the impeller shield, the hub, and the volute and other pump flow components. He pointed out that, under a low flow rate, the wear of the impeller shield is relatively large. With the flow rate increase, the wear of the blade pressure side and hub increases significantly. Pirouzpanah et al. (2019) studied the key parameters that affect the erosion phenomenon in the pump, such as turbulent kinetic energy, local sediment concentration, and near-wall relative sediment concentration velocity, and applied the results to the development of the prediction erosion model of the pump. Through experiments, Wang et al. (2022b) used five

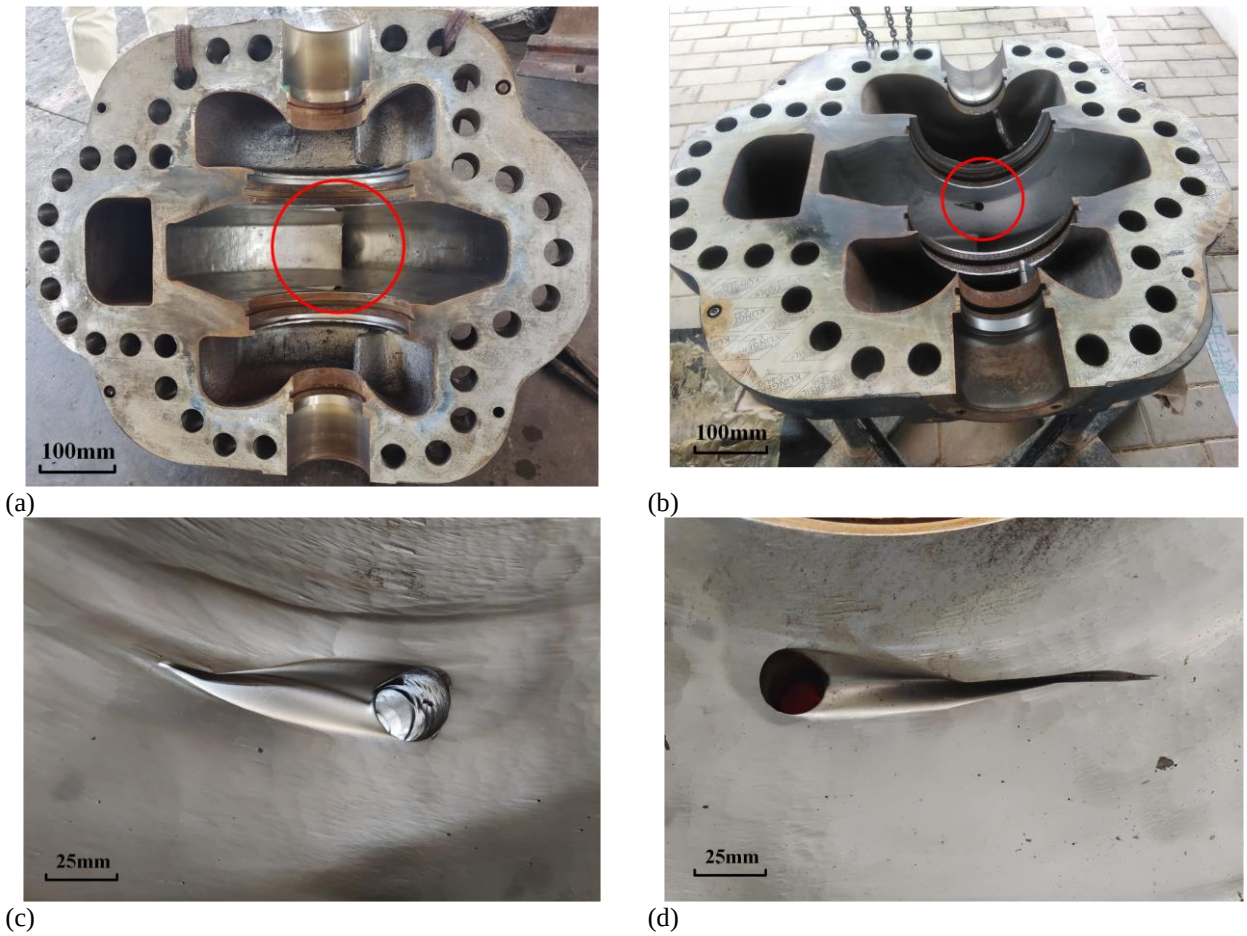


**Fig. 2 Erosion and wear morphology of pump casing (a) and (b), the Sulzer pump casing (c) and (d), the pump casing erosion wear details**

flow rates and three particle concentrations to carry out pump wear tests on the test bench. The head and efficiency of the centrifugal pump decreased with the increase in sediment concentration, while the effect of small sediment concentration on the energy performance of the pump was weak. Wang et al. (2022a) also verified using CFD that large particles of impurities have a greater impact on the performance decline of the centrifugal pump than small particles, and the increase of the overall proportion of large particles has a greater impact on the efficiency decline than the head drop. Sharma & Gandhi (2022) pointed out that the interaction of particles on the surface (such as sliding, rolling, and impacting at different angles) caused the impeller wear in the particle flow of the hydrodynamic machine by building the experimental platform. Song et al. (2021) used the Lagrangian particle tracking method and the Tabakoff erosion model to analyze the internal erosion of a double-suction centrifugal pump. They pointed out that the particle diameter affects the particle trajectory and significantly impacts the erosion shape and location in the impeller. Through experiments and CFD, Gomez-Flores et al. (2022) pointed out that erosion wear can reduce the speed and turbulence by reducing the volume of impeller blades and ultimately lead to the decline of centrifugal pump performance.

In summary, most of the current research on the internal flow channel erosion of centrifugal pumps is about the influence law of several factors on the degree of wear in the simulation, on the one hand, there is a lack of specific experimental support, and on the other hand, there is a lack of specific data to explain the influence law of solid particles' movement behavior on erosion, which makes the research results have limitations on the guidance of practical engineering. Based on the solid-liquid two-phase flow theory and numerical simulation technology, this study takes the Sulzer pump as the research object, carries out the simulation of the erosion wear of the internal flow channel of the pump, analyzes the erosion and wear characteristics of the centrifugal pump, explores the impact of the particle size of mechanical impurities and their mass flow on the erosion and wear, and expounds the wear mechanism of the pump casing from the perspective of particle motion law to provide guidance and suggestions for the stability and wear protection of Sulzer pump production and operation.

## 2. MATERIALS AND METHODS

### 2.1 Preparation of Test Samples

As shown in Fig. 3, a small sample was taken from the Sulzer pump casing for SEM and EDS detection. From Fig. 1. (b), it can be clearly observed that there are visible pits on the pump casing, which extend along the fluid direction. In order to meet the testing requirements, the surface of the sample is subjected to a certain degree of argon ion polishing and polishing. In this study, a metallographic grinder is used to polish the sample, an argon ion polishing machine is used to polish the sample, and finally, a scanning electron microscope (S-4800) is used to perform SEM and EDS testing on the pump casing sample.

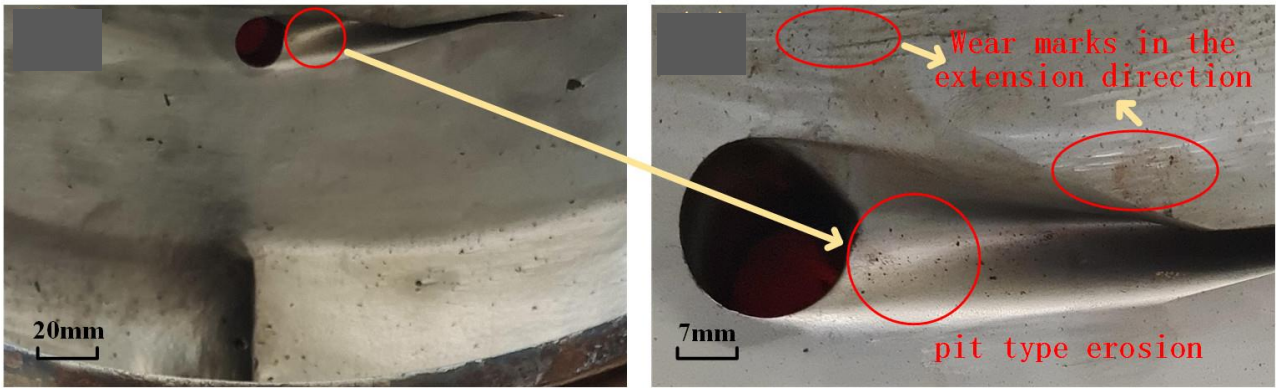


(a) (b)

**Fig. 3 Preparation of test samples**

### 2.2 Continuous Phase Model and Discrete Phase Model

During the transfer of oil by centrifugal pumps, solid particles (discrete phase) are entrained and transported by the fluid (continuous phase). There is mass, momentum and energy transfer between the particles and the fluid medium, and collisions also occur between the particles and between the particles and the solid walls. The solid-liquid two-phase flow in the pump during the transfer of oil by the centrifugal pump satisfies the mass conservation equation and the momentum conservation equation (Engin et al., 2001; Tarodiya & Gandhi 2017; Zhou et al., 2020), as shown in equation (1) and equation (2):

$$\frac{\partial}{\partial}\left(\sum_{k=1}^{n} a_k \rho_k\right)+\nabla\left(\sum_{k=1}^{n} a_k \rho_k \upsilon_k\right)=0 \tag{1}$$

$$\begin{aligned}&\frac{\partial}{\partial t}\left(\sum_{k=1}^{n} a_k \rho_k \upsilon_k\right)+\nabla\left(\sum_{k=1}^{n} a_k \rho_k \upsilon_k\right)=-a_k \nabla p\\&+\nabla\left[a_k\left(\tau_k^{'}+\tau_k\right)\right]\\&+a_k \rho_k g+M_k+\left(F_{\text{int}}\right)_k\end{aligned} \tag{2}$$

The discrete solution method is to search for each particle in the Lagrangian coordinate system, calculate the force due to contact, and then apply Newton's second law to calculate the variation of acceleration/velocity and displacement of the particle, and then obtain the state of the whole system. In solid-liquid two-phase flow, solid particles are mainly subjected to flow resistance, gravity, centrifugal force, Coriolis force, Basset force, and Magnus lift. The force control equation of solid particles is as follows ( Pagalthivarthi et al., 2011; Cai et al., 2016; ):

$$m_s \frac{du_s}{dt}=\frac{\pi d_s^3 \rho_s}{6}\left[\frac{g\left(\rho_s-\rho_f\right)}{\rho_s}+F_D+F_v+F_P+F_{other}\right] \tag{3}$$

Among them, $F_D$ , $F_v$ , $F_p$ , $F_{other}$ are shown in equations 4 to 8

$$F_D=C_D \cdot \frac{\pi d_p^2}{4} \cdot \frac{\rho_g\left(v_g-v_p\right)^2}{2} \tag{4}$$

$$F_v=-\frac{1}{2}\rho_g V_p \frac{dv_p}{dt} \tag{5}$$

$$F_p=-V_P \cdot \frac{\partial p}{\partial x} \tag{6}$$

$$F_{other}=\frac{1}{8}\pi p d_p^3\left(v-v_p\right)\omega+\frac{K_B}{4} d_p^2 \sqrt{\pi \rho_g \mu}\int_{t_0}^{t} \frac{\frac{d}{d\tau}\left(v_g-v_p\right)}{\sqrt{t-\tau}} d\tau \tag{7}$$

$$K_B=2.88+\frac{3.12}{\left(A_C+1\right)^3} \tag{8}$$

In the equation, $F_D$ is fluid flow resistance; $F_v$ is additional mass force; $F_p$ is additional force caused by pressure gradient $F_{other}$ is the sum of centrifugal force, Basset force, and Magnus lift. $C_D$ is drag coefficient; $V_p$ is Particle volume; $\omega$ is particle rotation angular velocity; $A_C$ is modulus of acceleration;

### 2.3 Erosion Model

When calculating erosion wear, an appropriate wear model must be introduced to predict the wear of the material surface. The present study applies the Finnie model (Emam et al. 2019; Ren et al., 2020). In the Finnie model, erosion varies with erosion angle and velocity: the specific calculation formula is as follows:

$$E=kV_p^n f(\gamma)$$

The model uses the following formula to relate erosion rate to particle impingement wall kinetic energy:

$$f(\gamma)=\begin{cases}\frac{1}{3}\cos^2\gamma & for\gamma>18.5^\circ\\ \sin(2\gamma)-3\sin^2\gamma & for\gamma\le 18.5^\circ\end{cases}$$

Where: $E$ is dimensionless erosion mass; $k$ is the model constant; $V_p$ is particle impact velocity; $f(\gamma)$ is non-variable function of angle of impact $(\gamma)$.

The model considers that the plowing and cutting effects of solid particles on the target surface are fully considered in the calculation, such as the mass of solid particles, the properties of the target material, and the

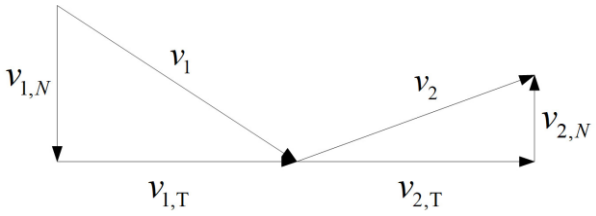


**Fig. 4 Schematic diagram of velocity vector before and after particle collision**

impact angle. The specific calculation formula is as follows:

$$\begin{cases} W = \dfrac{m_p u_p^2}{\sigma_f h_c K}\left(\sin 2\theta - \dfrac{6}{K}\sin^2\theta\right) & \tan\theta < \dfrac{K}{6} \\ W = \dfrac{m_p u_p^2}{\sigma_f h_c K}\left(\dfrac{K\sin^2\theta}{6}\right) & \tan\theta > \dfrac{K}{6} \end{cases} \tag{9}$$

The flow direction of the delivery medium of the Sulzer pump will change during transportation. The mechanical impurity particles the Sulzer pump carries will impact the wall surface and bounce along the inner surface many times owing to its own inertia. Figure 4 is the velocity vector diagram of the mechanical impurity particles before and after the collision. In this process, the particle rebound velocity will be smaller than the particle incident velocity, and the energy of solid particles will be lost and transferred, such as heat loss and material deformation on the wall (Tardiyaet al., 2019; Cornejo et al., 2021; Fan et al., 2020 ). Therefore, the velocity change before and after the collision between particles and the wall is accurately described by introducing the concept of particle wall rebound recovery coefficient, which represents the ratio of the normal velocity component before and after the collision and the ratio of the tangential velocity component before and after the collision, that is, the normal rebound recovery coefficient and the tangential rebound recovery coefficient.

$$\varepsilon_N = \frac{v_{2,N}}{v_{1,N}} \tag{10}$$

$$\varepsilon_T = \frac{v_{2,T}}{v_{1,T}} \tag{11}$$

The particle rebound model in this paper adopts the wall rebound recovery coefficient equation of Grant and Tabakoff (Moghimi & Rafee 2018):

$$\varepsilon_N = 0.993 - 1.76\alpha + 1.56\alpha^2 - 0.49\alpha^3 \tag{12}$$

$$\varepsilon_T = 0.998 - 1.66\alpha + 2.11\alpha^2 - 0.67\alpha^3 \tag{13}$$

### 2.4 Geometric Modeling and Condition Setting

Based on Sulzer pump drawings (as shown in Fig. 5), this study uses SolidWorks to model Sulzer pump impeller, pump casing, pump body, main shaft and other components. The 3D model is shown in Fig. 6. Some parameters of main components of Sulzer pump are shown in Table 1, and the working parameters are shown in Table 2.

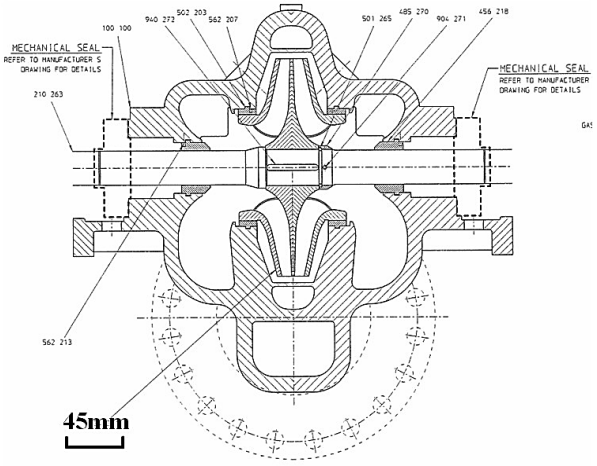


(a)

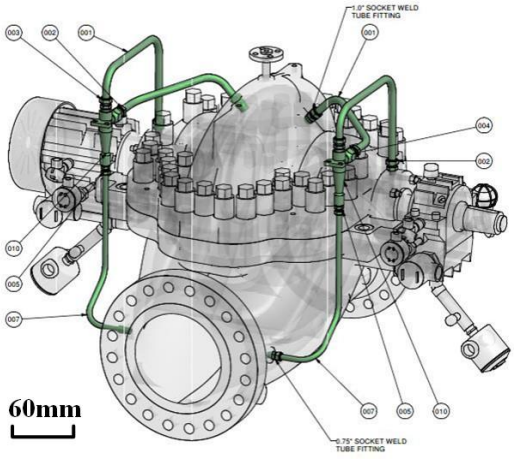


(b)

**Fig. 5 Part of Sulzer pump drawings (a) Cross-section view of Sulzer pump (b) Sulzer pump assembly**

**Table 1 Main structural parameters**

| Component | Parameter | Value |
|---|---|---|
| Impeller | Impeller outer diameter | 554(mm) |
| | Outlet Width | 72(mm) |
| | Number of blades | 6 |

**Table 2 Main working parameters**

| Machine | Parameter | Value |
|---|---|---|
| Sulzer pump | Rated flow | 1450($m^3$/h) |
| | Head | 400(m) |
| | Rated revolution | 2980(r/min) |

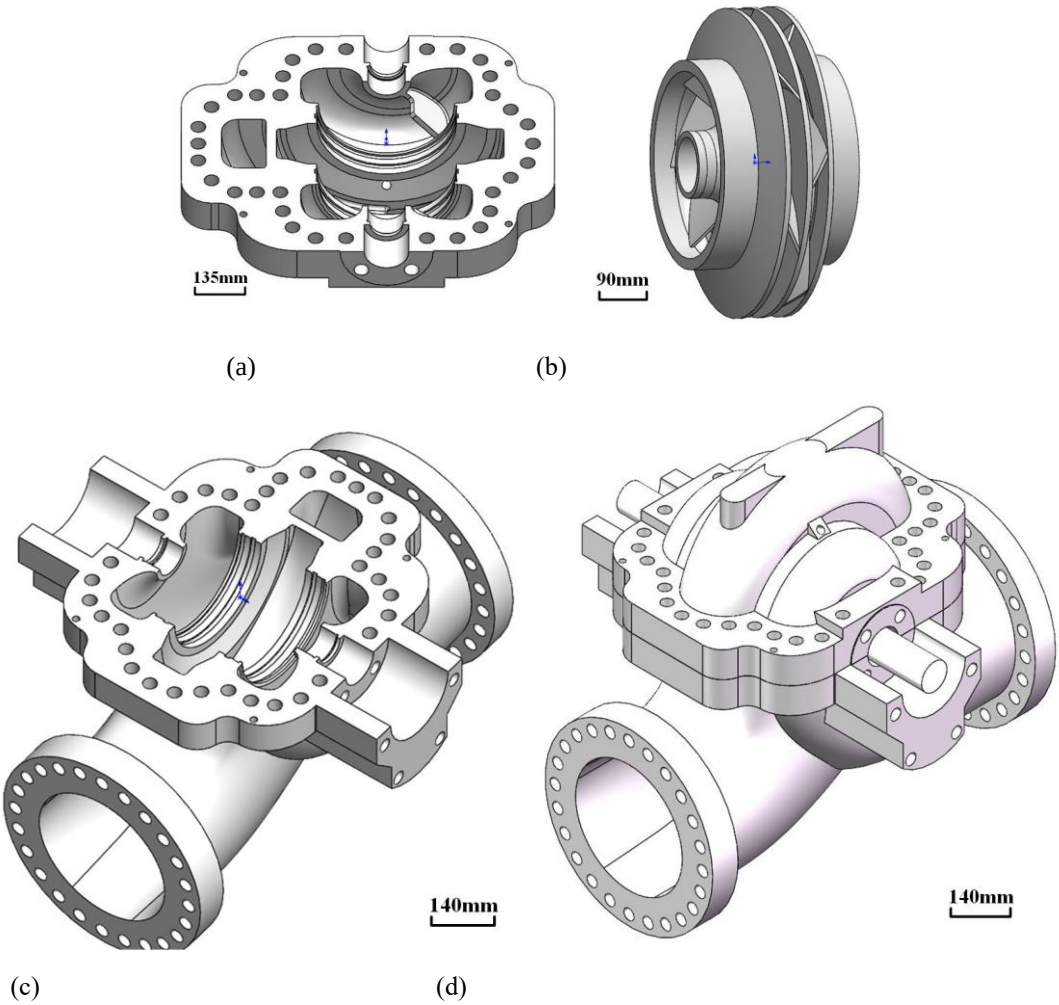


**Fig. 6 Three-dimensional model of Sulzer pump (a)Pump casing (b)Impeller (c) Pump body (d)Sulzer pump assembly model**

The fluid domain of the Sulzer pump is extracted by Boolean operation and then imported into ANSYS-Fluent. The fluid domain model of the Sulzer pump is shown in Fig. 7.

Combined with the Sulzer pump site conditions, the impeller and the main shaft set the Y-axis as the center of rotation, the rotational speed is set to 2980r/min, and the pump casing is fixed to its outer side. The inlet boundary of the pump casing is set as the pressure inlet, the inlet pressure is set as 3.8Mpa, the impeller outlet is set as the interface, and the fluid outlet of the pump casing is set as the outflow boundary, as shown in Fig. 8. The rest of the area is set as the wall. Liquid petroleum is selected as the conveying medium, and the parameters are kept as default.

Considering the nonlinear characteristics of the two-phase flow in the pump, the relaxation factors of pressure, density and volume force are set to 0.3, 0.5 and 0.5, respectively, and the relaxation factors of kinetic energy and turbulent kinetic energy are set to 0.6 and 0.8, respectively, and the reasonable setting of relaxation factors can accelerate the convergence time. The particle injection type is selected to be surface type, the initial distribution mode is selected to be diffuse distribution, and the wall condition is set to be reflect type. In the solution, the pressure, kinetic energy, and turbulent dissipation rate are discretized using the second order upwind format [26], the volume fraction is expressed in QUICK format, and the SIMPLEC algorithm is applied to the solution method.

### 2.5 Meshing and Irrelevance Verification

In numerical simulation, the number and density of grids will affect the accuracy and efficiency of calculation results, given the complexity of the geometric model of the object studied in this study. Sulzer's structural characteristics and site conditions are comprehensively considered. The curvature control function is selected for the advanced dimension function, and the unstructured tetrahedral mesh is used to mesh the three-dimensional model of the flow field. The parts, such as the mechanical seal flushing port and the impeller blade, are locally densified to enhance the reliability of the calculation results. At the same time, to reduce the dispersion error caused by the number of grids, six groups of grids with different numbers are used for calculation, and the maximum value of flow velocity and maximum erosion rate is used as the judgment basis for the independence analysis. As shown in Fig. 9, when the number of grids exceeds 2.1 million, the maximum velocity and erosion rate tend to be stable. Considering the calculation accuracy and solution resources, this study finally selects the fifth set of grids with several grids of approximately 2.1 million for subsequent calculation.

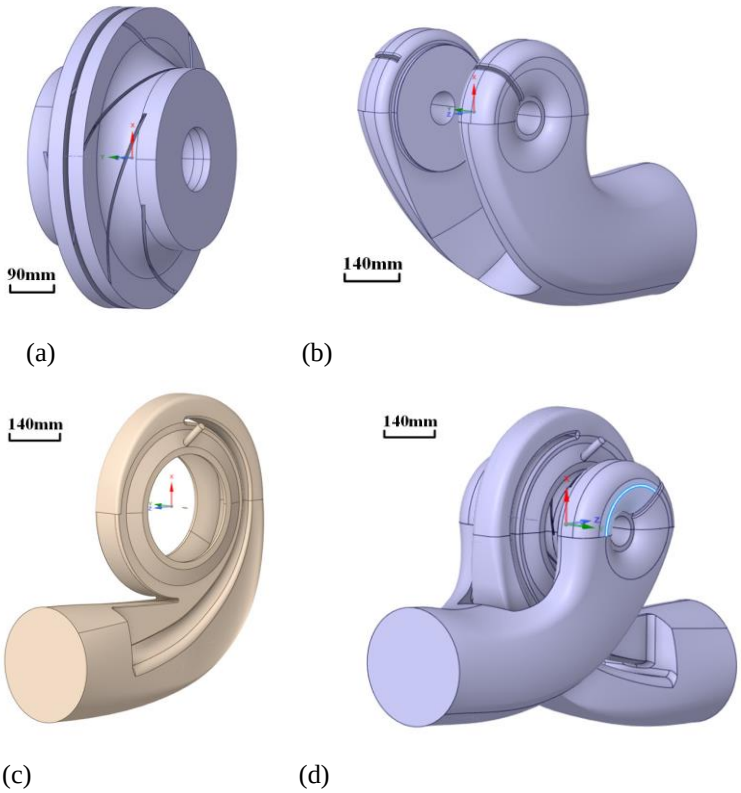


**Fig. 7 Sulzer pump fluid domain model, (a) Impeller (b)inlet flow path (c)outlet flow path(d)Sulzer pump integral fluid domain model**

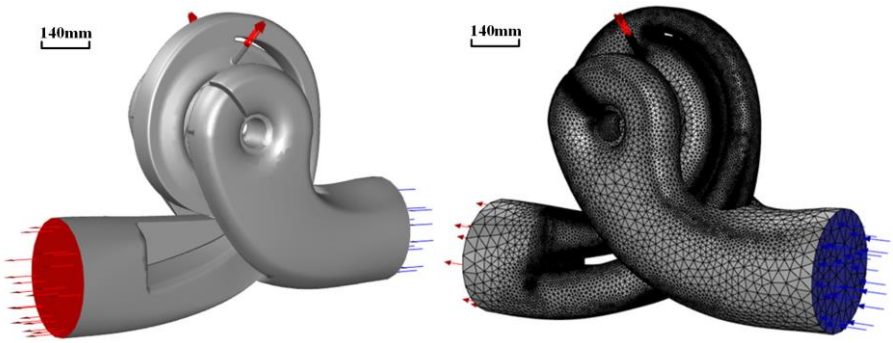


**Fig. 8 boundary condition**

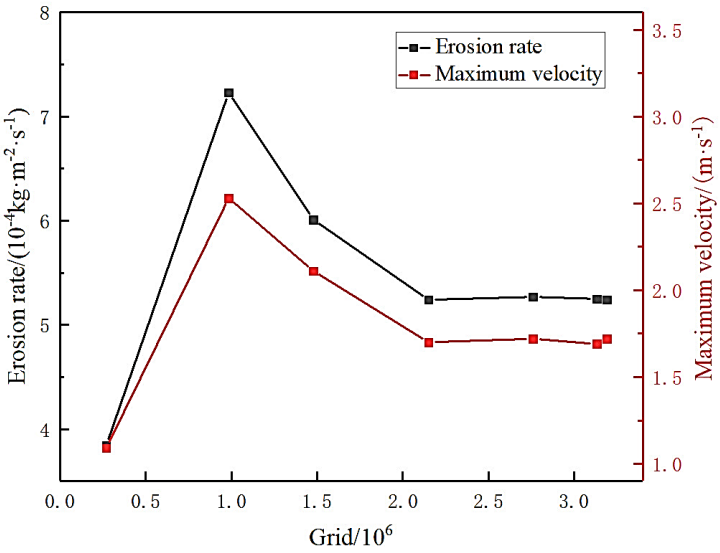


**Fig. 9 Grid independence verification**

**Table 3 Chemical composition of Q345 steel**

| Element | Fe | C | Si | Mn | Mo | S | Cu |
|---|---|---|---|---|---|---|---|
| Content （%） | 97.16 | 0.2 | 0.5 | 1.7 | 0.1 | 0.035 | 0.3 |

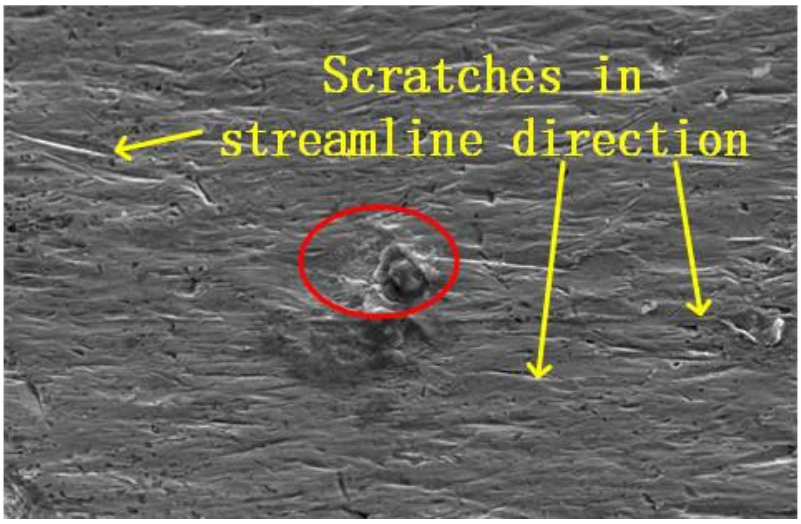


**Fig. 10 Low- magnification scanning image**

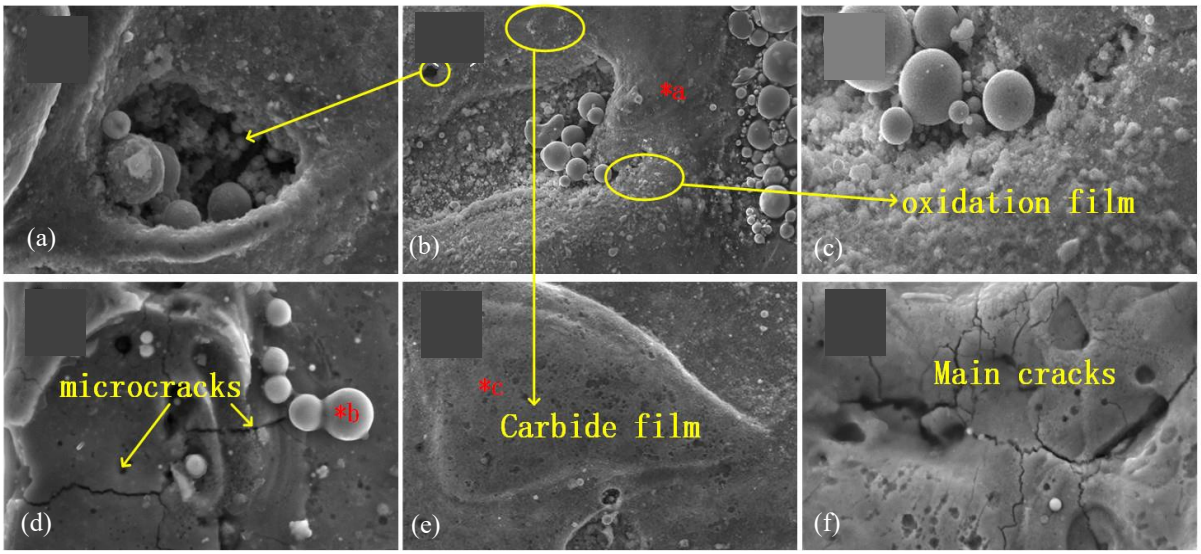


**Fig. 11 Electron microscope scanning results**

## 3. RESULTS

### 3.1 SEM and EDM Detection Results

The Sulzer pump casing is composed of Q345B steel, and the main components and content of Q345B steel are shown in Table 3.

Figure 10 shows the scanning electron microscopy (SEM) results of the sample. Numerous scratches can be seen on the surface along the streamline direction. The scratches may have been caused by the impurity particles in the conveying medium impacting the wall in a certain direction and with a certain velocity. A detailed observation was conducted on the region marked by a red circle in Fig. 10, and the results are shown in Fig. 11, which presents the local SEM morphology of the sample's surface. Figure 12 displays the energy-dispersive X-ray spectroscopy (EDS) results of the sample for three positions, which are labeled *a, *b, and *c in Fig. 10.

In Fig. 11 (b), a macroscopic observation was conducted of on the sample's surface was conducted at a lower magnification. It can be observed seen that the surface of the sample containss spherical particles of various sizes, as well as irregular small cracks and pits. Fig. 11 (f) shows presents a magnified view of one a prominent crack and, revealsing that the main crack is continuous and passes through multiple pitting points. Pitting points are also distributed at the end of the main crack, and smaller secondary cracks with shorter lengths and narrower widths extend from both sides of the main crack. An enlarged observation image of the secondary crack's' ends at the edge is shown in Fig. 11 (d). Smaller cracks can be observed extending outward from the secondary cracks, can be seen as well as along with the presence of pitting and spherical corrosion products. Unlike before, the development direction of the microcracks is irregular and often typically accompanied by pitting.

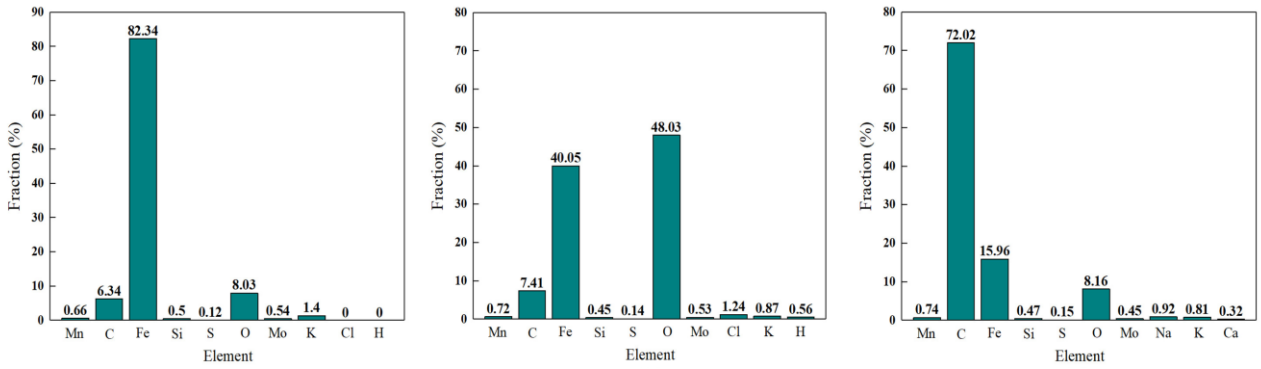


(a) (b) (c)

**Fig. 12 EDS analysis results**

Further observations were conducted on the surface pits in Fig. 11 (b). Figure 11 (a) presents a magnified SEM image of the left pit and reveals the presence of small spherical particles in the pit. Additionally, a magnified observation was conducted on the region containing numerous thin-film materials in the central part of Fig. 10 (b), and the results are shown in Fig. 11 (c). Various-sized spherical corrosion products can be seen in the pitting points. Figure 11 (d) *a presents the spherical particles near the microcrack, and Fig. 11 (b) *b presents the relatively intact surface location. EDS analysis was performed on the two locations, which correspond to Fig. 12 (a) and (b). From the results, it can be concluded that the spherical particles had a high oxygen content, which increased from 8.03% to 43.08%. Therefore, it can be assumed that the spherical particles consisted mainly of metal element oxides (Fe, Mn, Mo) from the pump casing. Furthermore, Cl (1.24%) and H (0.56%) were found in the spherical particles, which were not observed in the intact surface location. Therefore, it can be inferred that chloride ion corrosion occurred in the worn part of the pump casing. Figure 11 (e) presents the enlarged observation result of the dark and extensive film-like material above Fig. 11 (b). EDS analysis was conducted on the region, and the results are shown in Fig. 12 (c). Specifically, the proportion of the metal elements decreased, whereas the proportion of the oxygen elements remained relatively unchanged. The proportion of the carbon elements was the highest, which reached 72.02%, thereby indicating the presence of a carbon film. Previous research results also indicated the existence of numerous pitting points on the sample's surface. Figure 11 (c) shows the presence of fragmented oxides and an oxide film, which are typical characteristics of chloride ion corrosion. (Mao et al., 2022; Das et al, 1999).

In conclusion, severe chloride ion corrosion occurred in the worn part of the pump casing. The conveying medium in the Sulzer pump contains formation water and production-enhancing chemicals, which contain a considerable amount of chloride ions and acidic substances. When the protective film on the pump casing surface is damaged, the chloride ions on the exposed metal surface will likely be adsorbed. Differences may exist between the ionic, exposed metal surface, and protective film models; thus, a galvanic cell will be formed (Demeneghi et al., 2022). Consequently, the exposed metal in this area will be highly prone to corrosion. The corrosion products generated in the area are transported continuously, leading to the ongoing corrosion process and continuous enlargement of the pitting points and accelerating the wear on the pump casing.

Additionally, K, Ca, and other elements are detected in the EDS results for the three locations. This finding indicates that during the crude oil transportation process, mechanical impurities collide continuously and remain inside the pump casing, because C, K, Na, and Ca are the main components of mechanical impurities and scale deposits in oil pipelines. In summary, the pipeline used in the Sulzurshou pump contains scale deposits and mechanical impurities, which continuously impact the internal surface and cause local coating damage. After the metal inner surface was exposed, a galvanic cell is formed between the chloride ions and hydrogen ions in the crude oil, thereby accelerating the corrosion in the area. Additionally, the constant impact of the solid-liquid two-phase flow contributes to the severe erosion wear on the inner surface of the Sulzurshou pump casing. The next section discusses the kinematic behavior of the particulate impurities inside the pipeline and explores the erosion wear mechanism on the pump in detail.

### 3.2 Erosion and Wear Characteristics of Sulzer Pump

The impact of high-speed solid-liquid two-phase flow from the impeller of the centrifugal pump on the inner surface of the pump casing is the direct cause of erosion wear failure. The flow field characteristics in the pump will greatly affect the kinematic behavior of solid particles (Fuyan & Hesheng, 1991; Padhy & Saini 2011). To explore the erosion and wear characteristics of the centrifugal pump, this section analyzes the flow law in the flow field of the Sulzer pump under operating conditions and the movement behavior of mechanical impurity particles.

Figure 13 shows the static pressure and speed comparison of the Sulzer pump's flow field comparison diagram under pure liquid and mechanical impurity conditions at the same flow rate. The flow field laws of the two are roughly the same. The static pressure value of the impeller of the Sulzer pump gradually increases along the radial direction of the impeller, and the value of the pressure surface of the impeller is significantly greater than the suction surface, indicating that the power capacity of the impeller continues to increase from the inlet to the outlet of the impeller. The presence of mechanical impurities makes the inlet and outlet pressure of the impeller lower, and the distribution of the velocity field has no apparent difference.

Figure 14 is the distribution diagram of the liquid phase trace of the Sulzer pump. As shown in the figure, when the Sulzer pump is running, the flow vortex at the middle passage of the impeller is irregular. The unstable vortex is the reason for large hydraulic efficiency loss (Forder et al.,1998), which explains the phenomenon of large hydraulic loss at a low flow rate. Given the dynamic and static interference between the impeller and the pump casing, the Sulzer pump has a maximum velocity gradient at the impeller outlet under all operating conditions.

As shown in Fig. 15, vortex generation is most obvious in low-flow conditions. With the increase of flow (for example, 1.0Q, rated flow of Sulzer pump 1.0Q=1450 m3/h), the area of vortex decreases, and the relative velocity gradient of fluid decreases, but the vortex area still exists. The increased flow rate raises the fluid velocity, and the area with a low flow rate drops.

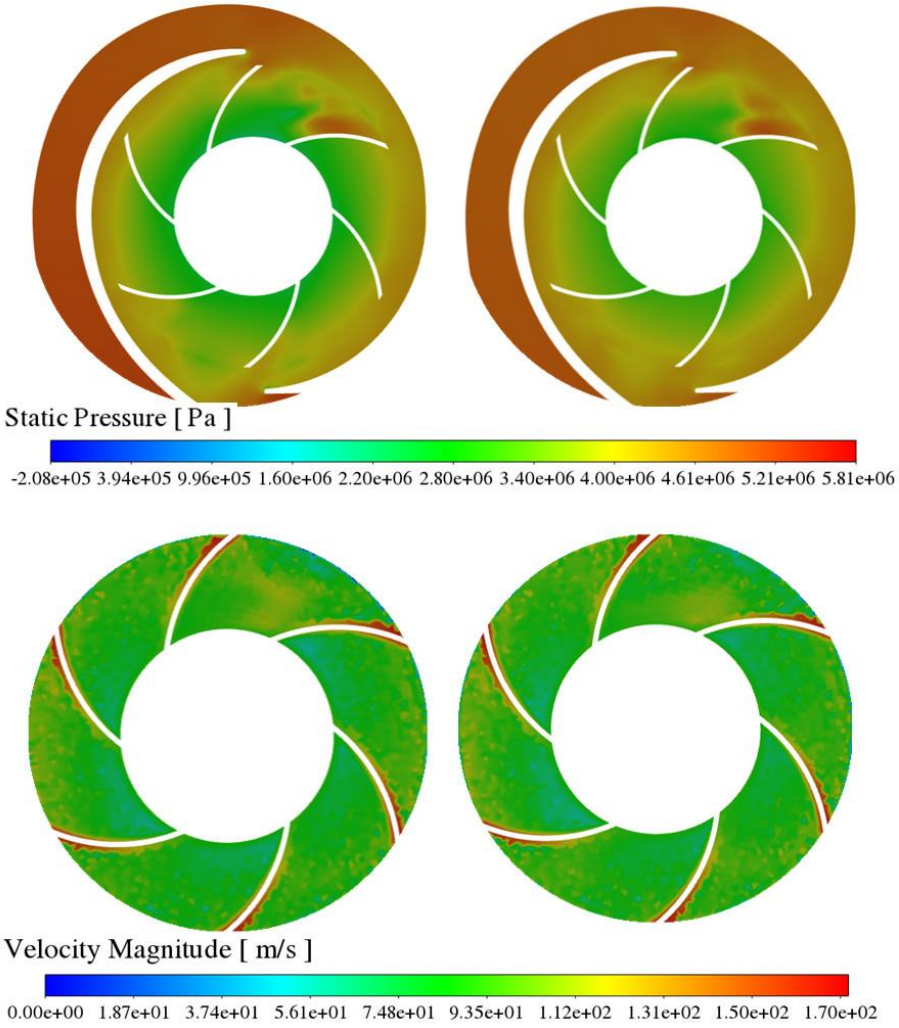


**Fig. 13 Flow field comparison diagram of pure fluid and solid-liquid mixed phase of Sulzer pump (left: pure fluid, right: solid-liquid two-phase flow)**

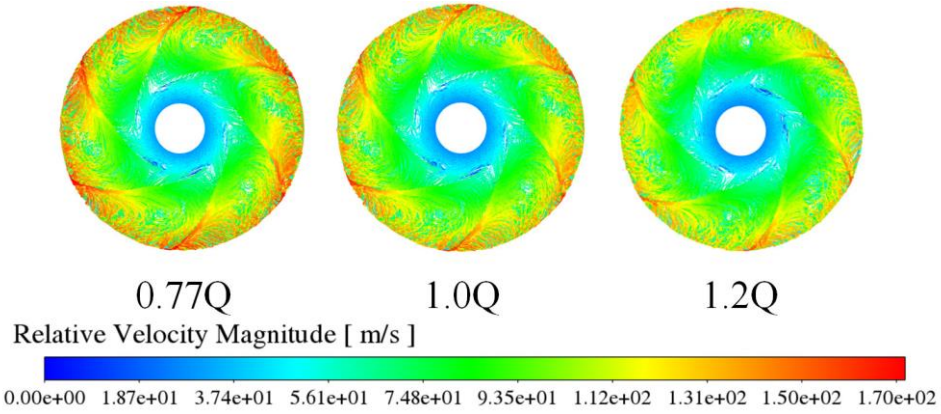


**Fig. 14 Trace distribution of flow field inside Sulzer pump**

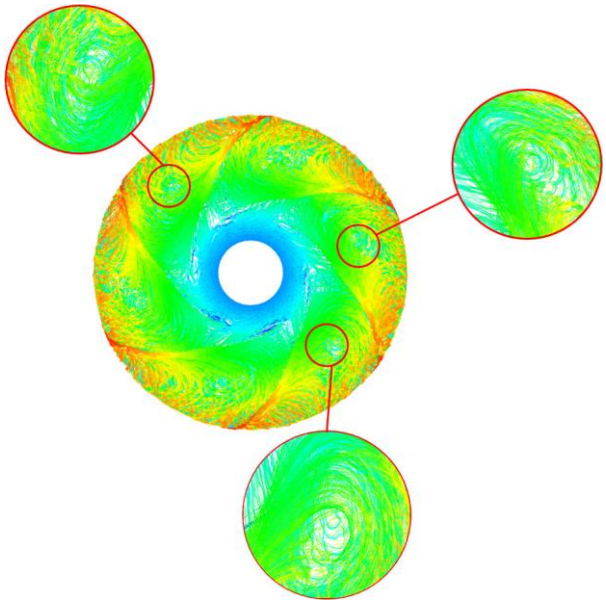

**Fig. 15 Vortex area at impeller outlet**

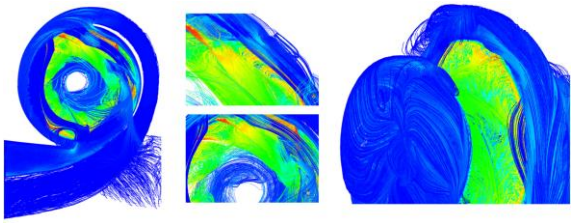

**Fig. 16 Trace comparison diagram of the Sulzer pump under pure fluid and solid-liquid two-phase conditions**

Figure 16 shows that, under the influence of mechanical impurities, the flow field in the impeller of the Sulzer pump presents a more pronounced gradient distribution, and the low-speed vortex area is also more apparent. The figure presents that this area is closer to the inlet of the impeller. This phenomenon may be caused by the high-speed rotation of the impeller when entering the impeller, making the fluid obtain a certain amount of energy near the back of the blade and thus causing the flow separation near the wall of the inlet. From the inlet to the outlet, the flow separation phenomenon is becoming increasingly serious, thus generating a certain degree of backflow and generating a vortex. However, the larger inertia of particles makes their following ability weaker than that of the fluid medium, which makes the particles have a certain delay process in the movement of the fluid, which makes the low-pressure vortex area further larger, and the increase of the particle velocity difference also causes a certain degree of wear on the blade wall.

Figure 17 shows the stress distribution on the impeller wall of the Sulzer pump under rated conditions. The impeller has good control of incoming water flow, and its impeller pressure distribution is roughly uniform. Moreover, the front impeller pressure is higher than that at the back under the same radius. At the same time, because the impeller blades work on the medium passing through the impeller, the flow surface pressure distribution is gradually increasing from the impeller inlet to the outlet along the flow direction. The pressure

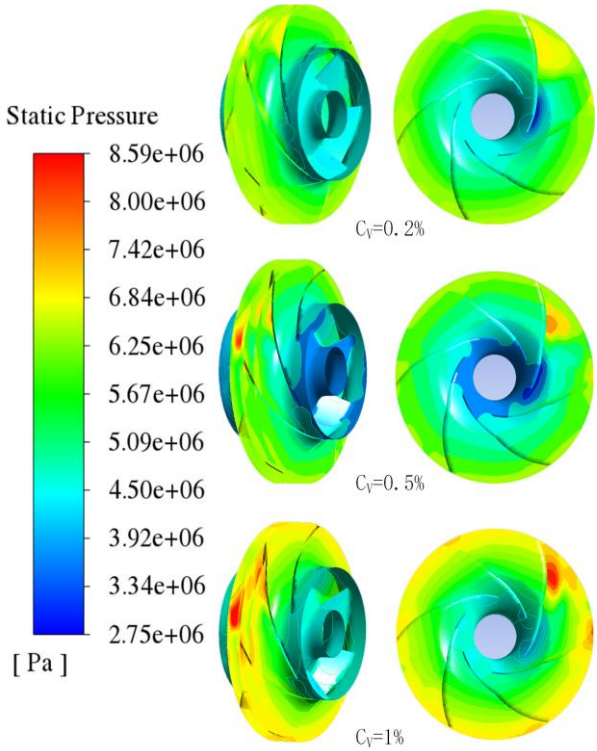


**Fig. 17 Impeller stress cloud chart**

distribution of the centrifugal pump impeller also reflects the influence of the volute tongue structure on the flow field of the centrifugal pump impeller. That is, the pressure at the outlet of the impeller blade passage near the volute tongue is significantly higher than that at the outlet of other blade passages, which indicates that the flow field near the volute tongue is distorted owing to the relative movement of the impeller blade and the volute tongue.

Under different solid concentration conditions, the pressure distribution in the impeller of the Sulzer pump presents a similar law, and the pressure gradually increases from the inlet to the outlet. With the increase of solid concentration, the low-pressure area near the back of the blade in the tangential direction of the impeller inlet gradually increases because some large particles collide with the impeller inlet and stall into the pressure surface flow channel and then accelerate under the action of the impeller rotating centrifugal force. In this process, the higher the solid concentration, the more pressure energy is lost in the acceleration process, resulting in the gradual increase of the low-pressure area.

As shown in Fig. 18, the wear position of the centrifugal pump impeller is mainly distributed in most parts of the blade working surface, and the closer to the outlet position, the more serious the wear of the blade. The reason may be the mechanical impurity particles colliding with the impeller inlet and entering the impeller flow channel after stalling. Under the same centrifugal force, the smaller the acceleration of the larger particles, the longer the time it takes to move to the back of the blade (Penga et al., 2020), and the closer it is to the back of the blade outlet, resulting in increased wear at the back of the blade outlet. When the small particles move in the flow channel, they will carry more energy to the working surface of the blade, resulting in serious wear here.

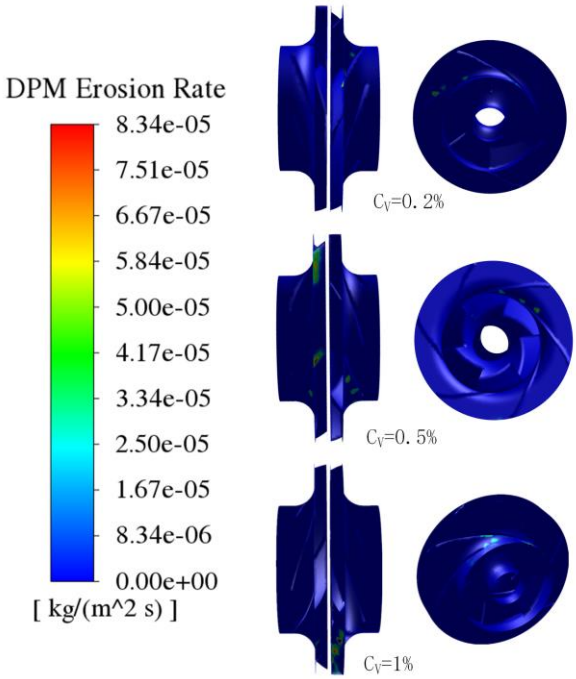


**Fig. 18 Cloud chart of Impeller Erosion and Wear under Different Solid Concentration**

Under actual operating conditions, the fluid flows out of the impeller at high speed under centrifugal force and enters the flushing port from the end of the pump casing. Figures 19 and 20 show that the fluid velocity in the pump casing is relatively uniform, whereas the fluid velocity in the pipe is relatively disordered and its maximum velocity is on the right wall of the pipe. The main reason is the flow and pressure difference between the fluid in the pipe and the inlet section and the maximum velocity of the fluid flowing to the flushing port are biased to the side pipe wall owing to the influence of the diversion belt. The pressure of the fluid increases suddenly at the diversion point. The wall surface at the intersection of the pump casing and the branch pipe appears to be a high-pressure area owing to the direct impact of the fluid, and the pressure in the pump casing is large and almost unchanged. However, the pressure in the pipe is relatively low, and the pressure at its upper end is reduced owing to the eddy current phenomenon. The reason for this phenomenon is that the fluid is subject to the centrifugal force in the process of flowing from the pump casing into the pipe, resulting in the spiral of the fluid in the pipe (Mortazavi et al., 2017), which causes low pressure inside.

As can be seen from the particle erosion wear cloud Fig. 21, the most serious abrasion area is the right side of the flushing port and the pump casing, and the erosion and abrasion rate reaches $5.94 \cdot 10^{-4}$ kg·m$^{-2}$·s$^{-1}$, which is much more serious than that of the impeller (8.59·10-6 kg·m$^{-2}$·s$^{-1}$).Under the joint action of turbulent diffusion and fluid adhesion (Rajani et al., 2012; Bai et al., 2019), particles enter into two flow channels. Some particles flow to the outlet of the flushing port with the fluid, and the other particles flow to the outlet flow channel of the pump casing owing to the inertia. The particles in the flow

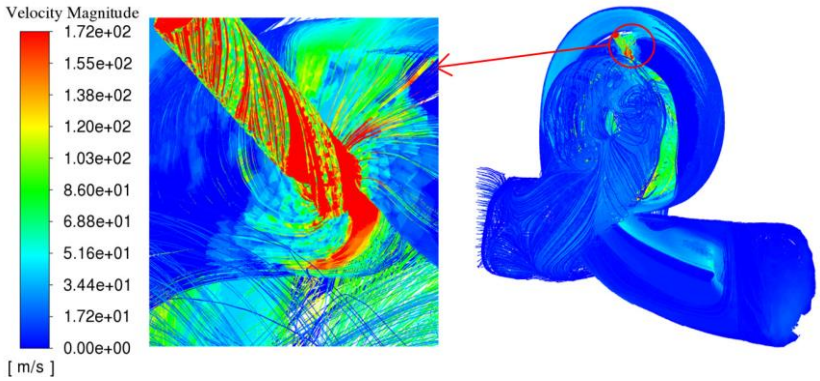


**Fig. 19 Cloud diagram of the fluid velocity at the branch pipe of the flushing outlet**

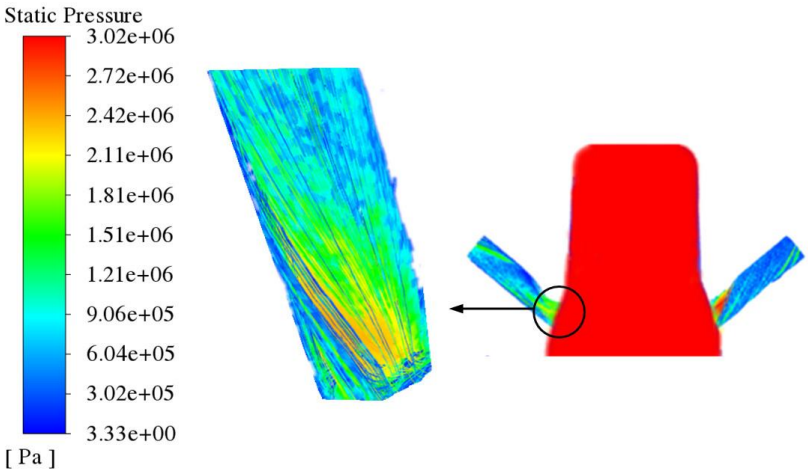


**Fig. 20 Pressure cloud chart at flushing outlet branch pipe**

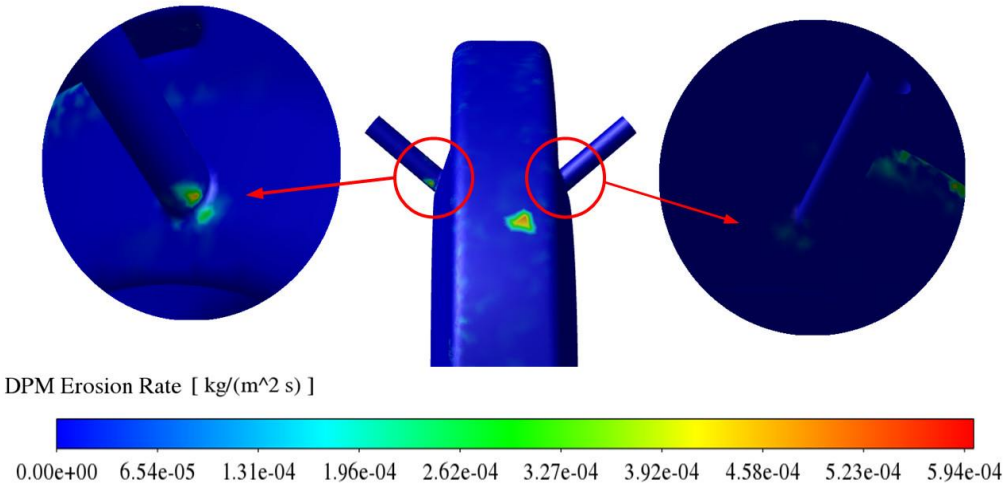


**Fig. 21 Cloud chart of wear rate of mechanical seal flushing port under actual working conditions**

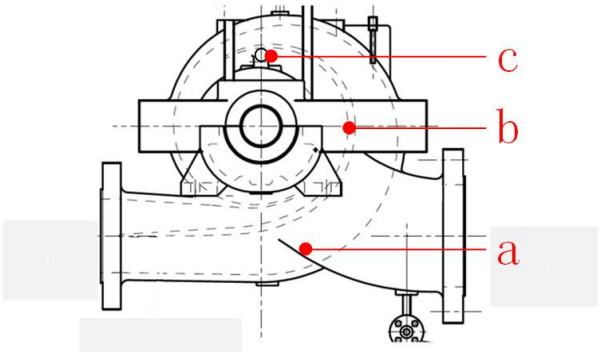


**Fig. 22 Location of Sulzer pump monitoring points**

channel of the flushing port directly impact the right side of the branch pipe as the fluid flows to the flushing port and flows out of the flushing port outlet with the fluid eddy current, causing erosion and wear on the pipe wall surface. Some particles flowing to the outlet channel of the pump are affected by the diversion, and their velocity direction is shifted to the lower side of the flushing port. They collide with the pump casing wall to cause erosion and wear. The collision location is concentrated in the area close to the intersection line, consistent with the actual situation.

### 3.3 Influence of Impurity Particle Size on Erosion Wear of Sulzer Pump

According to the previous research results, mechanical impurities particles will impact the flow field in the pump, and their own properties and movement rules will directly affect the erosion wear in the Sulzer pump. Based on the principle of a single variable, this section analyzes the influence of particle size of mechanical impurities on erosion wear. As shown in Fig. 22, the following monitoring points prone to erosion and wear are set in the Sulzer pump: (a) pump inlet path, (b) impeller blade, and (c) mechanical seal flushing port.

The Sulzer pump has a 20-mesh filter, and the maximum particle size is 0.85 mm. The pump inlet is set as the working pressure, and different particle sizes are set to simulate erosion and wear.

The calculation results are shown in Fig. 23, with the increase of particle size, it can be found that the maximum erosion rate of each monitoring point shows a gradually increasing trend with the increase of particle size. When the solid particle size is 0.1mm, the maximum erosion rates of the inlet flow channel, impeller blades, and mechanical seal flushing port are $0.24\cdot10^{-11}$ $kg\cdot m^{-2}\cdot s^{-1}$, $0.212\cdot10^{-4}\cdot kg\cdot m^{-2}\cdot s^{-1}$ and $0.76\cdot10^{-4}$ $kg\cdot m^{-2}\cdot s^{-1}$, respectively, and when the solid particle size is 0.3mm, they have values of $0.742\cdot10^{-11}$ $kg\cdot m^{-2}\cdot s^{-1}$,$0.62\cdot10^{-4}$ $kg\cdot m^{-2}\cdot s^{-1}$, $2.3\cdot10^{-4}$ $kg\cdot m^{-2}\cdot s^{-1}$, respectively. When the solid particles are 0.5 mm, their values are $0.856\cdot10^{-11}$ $kg\cdot m^{-2}\cdot s^{-1}$,$1.84^{-4}\cdot kg\cdot m^{-2}\cdot s^{-1}$, $5.4^{-4}\cdot kg\cdot m^{-2}\cdot s^{-1}$, When the solid particles are 0.7 mm, their values are $1.83\cdot10^{-11}$ $kg\cdot m^{-2}\cdot s^{-1}$,$2.55\cdot10^{-4}$ $kg\cdot m^{-2}\cdot s^{-1}$, $5.9\cdot10^{-4}$ $kg\cdot m^{-2}\cdot s^{-1}$. when the solid particle size is 0.85mm, they have values of $2.52\cdot10^{-11}$ $kg\cdot m^{-2}\cdot s^{-1}$,$3.21\cdot10^{-4}$ $kg\cdot m^{-2}\cdot s^{-1}$, $6.7\cdot10^{-4}$ $kg\cdot m^{-2}\cdot s^{-1}$, respectively. And it can seen that the inlet path of the pump casing has undergone erosion wear to a certain extent. The result of the average particle size of 0.85 mm is nearly 10 times higher than that of 0.1 mm, and the change rate of each group is also different. The larger the particle size is, the greater the impact on the erosion wear rate of the inlet passage will be. Figures 23 (b), 23 (c), and 23 (d) show that the impeller blade and the flushing port have undergone severe erosion wear, of which the flushing port has the most severe erosion wear, and the maximum erosion wear rate has reached $6.7\times10^{-4}kg\cdot m^{-2}\cdot s^{-1}$. Moreover, when the particle size increases from 0.1 mm to 0.5 mm, the change rate of the maximum erosion wear rate at the flushing port is greater. As the particle size continues to increase, the increase rate of the maximum erosion wear rate significantly reduces. Compared with the other two monitoring points, the erosion and wear of the inlet channel are relatively light, which is also in line with the actual field observation results. Within the mass flow range of the impurity particles in this model, the volume fraction of the mechanical impurity particles relative to the fluid medium transported in the pipeline is small. The numerical simulation data of each group at the monitoring point show that the increase in particle size has little effect on the maximum flow velocity of the flow field in the pump. From the side, the change in the maximum erosion rate has nothing to do with the change of the maximum flow velocity in the flow field caused by the particle size change.

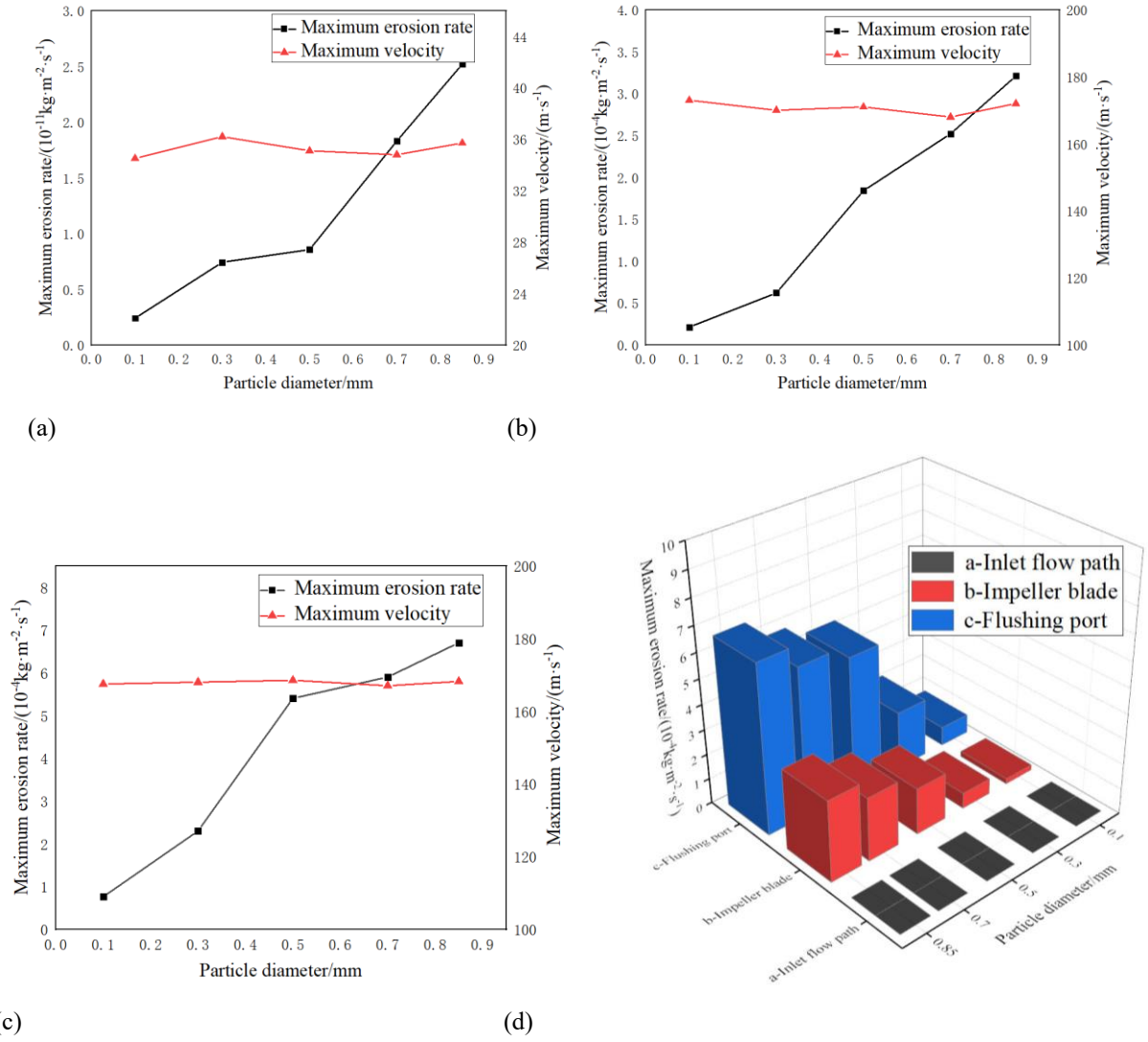


**Fig. 23 Simulation results (a) a monitoring point (inlet flow path) (b) b monitoring point (impeller blade) (c) c monitoring point (mechanical seal flushing port) (d) Comparison of maximum erosion rate data**

## 4. DISCUSSION

According to Section 3, the erosion wear of the Sulzer pump surface is mainly caused by the interaction between small particles of mechanical impurities and the wall surface during the oil transportation process. At the same time, the movement behavior of impurity particles will be affected by the flow field characteristics in the pump, thus affecting the extent and location of erosion wear in the pump. The locations where erosion wear is easy to occur in the pump include the wall surface of the pump inlet passage and the blade at the impeller outlet. At the mechanical seal flushing port above the pump casing, the wall erosion at the inlet is the most serious, followed by the blade at the impeller outlet. Moreover, there are other areas with slight erosion and low wear. This section synthesizes the previous simulation results to explore the causes and mechanisms of wall wear at various parts of the Sulzer pump.

According to the previous research results, a certain degree of erosion and wear occurred on the wall of the pump inlet path, and with the increase of particle size, the degree of wear in this area will increase. The larger the particle size, the greater the acceleration speed of erosion and wear in the inlet path, as shown in Figs 23 (a) and 24. This phenomenon is caused by the transport medium being sucked into the impeller after passing through the inlet channel, and the movement direction in the annular space at the inlet changes from linear to circular motion, as shown in Fig. 25. Impurity particles are affected by their inertia force and the centrifugal force of the impeller and will impact the wall at the entrance passage at a certain speed and angle, which also causes erosion and wear here. When the average particle size of the impurity particles increases, the greater the inertia force, the easier it is to hit the wall of the inlet channel, and the more serious the collision is.

When analyzing the wear of the inlet passage of the pump casing, slight wear was also found at the top and outlet sections of the pump casing, which was caused by the small impurity particles, owing to the small inertia force, and the good follow-up with the fluid, which would lag behind the large particles to collide with the inner wall of the pump casing, as shown in Fig. 25.

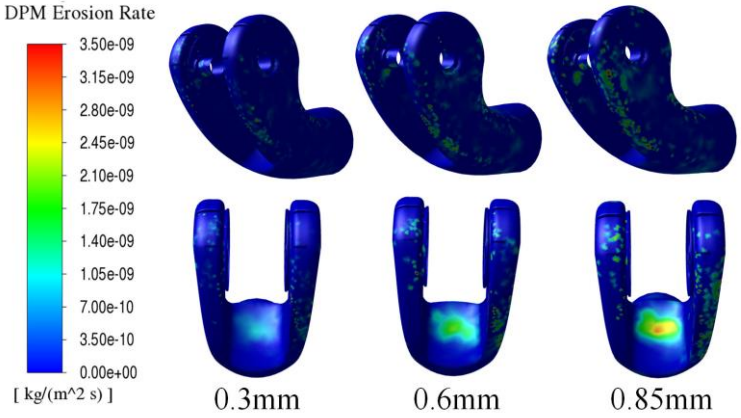


**Fig. 24 Erosion cloud chart of the inlet channel under different particle sizes**

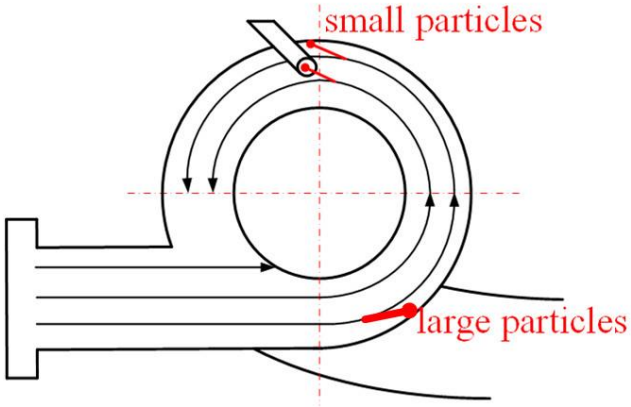


**Fig. 25 Schematic diagram of particle motion track**

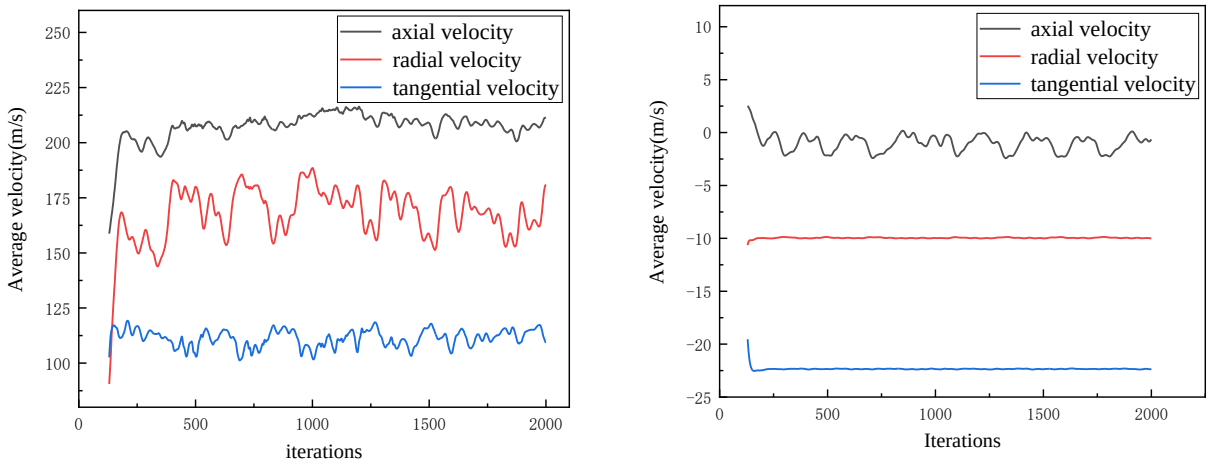


(a) (b)

**Fig. 26 Average velocity data of different monitoring points (a) Mechanical seal flushing port and (b) Sulzer pump outlet path**

There is a pressure difference between the mechanical seal flushing port above the pump casing's inner surface and the pump's high-pressure fluid. When the solid-liquid two-phase flow passes through this position, part of the fluid will be squeezed into the flushing channel. Setting monitoring points in this area, as shown in Fig. 26 (a), the fluid in the pump has a certain axial velocity, and its size is even larger than the radial and tangential velocities. Then, comparing the data of the Sulzer pump outlet flow channel monitoring points, as shown in Fig. 26 (b), the tangential and radial velocities in this area are negative because the flow direction changes when the fluid passes through various flow parts in the pump. The figure shows that the tangential velocity of the fluid in this region is the largest, the value is stable at approximately 25 m/s, and the minimum is the axial velocity, which fluctuates from 0 to 2 m/s. The axial velocity in the flushing channel area is too large, which constitutes the local eddy current at the flushing port of the Sulzer pump mechanical seal. The generation of local eddy current makes the impurity particles under the combined action of centrifugal force and fluid drag force,

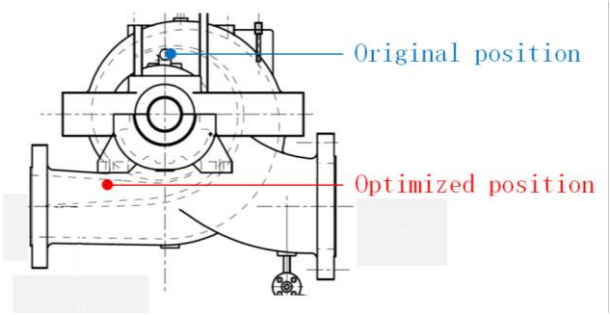


**Fig. 27 Schematic diagram of optimized location of mechanical seal flushing port**

the smaller particles will continuously collide with the wall of the flushing port, and the collision location is concentrated in the area close to the intersection line, causing serious erosion and wear.

To sum up, given the inevitable high-pressure difference between the flushing port and the impeller outlet, local vortices and serious interference between them are caused, and the impurity particles will continuously impact the blade surface and the pump inner surface. To avoid rapid erosion and wear in the pump casing, the following measures are recommended:

1. HVOF coating shall be applied to the surface of impeller blades and shell flow passage parts to improve the surface hardness and wear resistance of flow passage parts.

2.As Fig. 27 shown, for the optimization and modification of the mechanical seal flushing hole, the position of the mechanical seal flushing hole on the original pump casing is at the top of the shell directly opposite the blade outlet, with a high flow rate and large impact. The position of the pump body outlet flange neck should be modified to reduce the impact of high-speed fluid erosion and weld the original pump body mechanical seal flushing hole.

## 5. CONCLUSIONS

This research focuses on an oil delivery Sulzer pump in a completed oil pipeline. The erosion and wear conditions and direct causes are determined using SEM and EDS. Then, the internal flow field characteristics and wear properties are analyzed using the CFD-DPM coupled model. The main conclusions of this study are as follows:

- The deposits and mechanical impurity particles inside the pipeline impact the pump casing surface with a certain velocity and angle, causing local coating damage. After the metal inner surface was exposed, the chloride ions and hydrogen ions in the crude oil form a galvanic cell with the metal, thereby accelerating the corrosion in the location at the microscopic level. In addition, the interaction of the high-speed solid-liquid two-phase flow leads to the severe erosion and wear on the Sulzer pump.
- The static pressure and fluid velocity inside the pump increase gradually along the radial direction of the impeller and reach the maximum value at the impeller outlet. Flow vortices appear in the pump impeller outlet flow channel, and this phenomenon worsens as deviation from the rated flow rate increases. The unstable flow vortices cause the hydraulic efficiency loss and affect the motion behavior of the solid particles in the area. As the impurity particle concentration increases, the flow field distribution inside the pump will show a highly significant gradient, and the vortex region will become highly pronounced.
- The inlet flow channel of the Sulzer pump experiences slight erosion and wear. The reason for this outcome is that the motion mode of the solid-liquid two-phase flow changes when it passes through the area, and the large-sized impurity particles in the fluid will impact the wall surface owing to their inertia. The maximum erosion rate of the inlet flow channel wall will exhibit an increasing trend as the particle size increases, and the larger the particle size, the greater the impact on the erosion and wear rate of the inlet flow channel.
- The impeller and mechanical seal flushing port of the Sulzer pump experience severe erosion and wear. The reason for this outcome is the high pressure difference between the impeller outlet and flushing port inlet. The high-pressure and high-velocity fluid ejected from the impeller will experience axial pressure and flow continuously into the flushing port. Under the combined action of turbulent diffusion and fluid adhesion, some particles deviate from their velocity direction and collide constantly with the pump casing wall, thereby causing erosion and wear.
- The maximum erosion rate of the flushing port reaches $6.7\times10^{-4}$ kg·m$^{-2}$·s$^{-1}$. When the particle size increases from 0.1 mm to 0.5 mm, the variation rate of the maximum erosion rate of the flushing port will increase. As the particle size continues to increase, the magnitude of the increase in the maximum erosion rate will become significantly small.

## CONFLICT OF INTEREST

The authors declare that they have no known competing financial interests or personal relationships that could have appeared to influence the work reported in this paper.

## AUTHORS CONTRIBUTION

**L. F. Qiao**: Data analysis and Writing; **L. Mo**: Validation; **L. J. Mao**: Supervision; **J. L. Zhu**: Data Curation; **L. X. Zeng**: Data Curation.

## REFERENCE

Bai, L., Zhou, L., Han, C., Zhu, Y., & Shi, W. (2019). Numerical study of pressure fluctuation and unsteady flow in a centrifugal pump. *Processes*, *7*(6), 354. https://doi.org/10.3390/pr7060354

Cai, X., Zhou, S. P., & Li, S. (2016, May). *Study on the influence of back blade shape on the wear characteristics of centrifugal slurry pump.* IOP Conference Series: Materials Science and

Engineering. IOP Publishing. https://10.1088/1757-899X/129/1/012058.

Chandel, S., Singh, S. N., & Seshadri, V. (2012). Experimental study of erosion wear in a centrifugal slurry pump using coriolis wear test rig. *Particulate Science and Technology*, *30*(2), 179-195. https://doi.org/10.1080/02726351.2010.523926.

Cornejo MacEda, G. Y., Li, Y., Lusseyran, F., Morzyński, M., & Noack, B. R. (2021). Stabilization of the fluidic pinball with gradient-enriched machine learning control. *Journal of Fluid Mechanics*, *917*, A42. https://doi.org/10.1017/jfm.2021.301

Das, G., Sinha, A. N., Mishra, S. K., & Bhattacharya, D. K. (1999). Failure analysis of counter shafts of a centrifugal pump. *Engineering Failure Analysis*, *6*(4), 267-276. https://doi.org/ 10.1016/S1350-6307(98)00037-5.

Demeneghi, G., Rodgers, K., Su, C. H., Medders, W. M., Gorti, S., & Wilkerson, R. (2022). Root cause analysis of premature simulated life cycle failure of friction stir welded aluminum 2219. *Engineering Failure Analysis*, *134*, 106059. https://doi.org/10.1016/j.engfailanal.2022.106059

El-Emam, M. A., Shi, W., & Zhou, L. (2019). CFD-DEM simulation and optimization of gas-cyclone performance with realistic macroscopic particulate matter. *Advanced Powder Technology*, *30*(11), 2686-2702. https://doi.org/10.1016/j.apt.2019.08.015.

Engin, T., Gur, M., & Calli, I. (2001). *Slurry and tip clearance effects on the performance of an open impeller centrifugal pump.* Handbook of Powder Technology. Elsevier Science BV. https://doi.org/10.1016/S0167-3785(01)80052-X

Fan, D., Zhang, B., Zhou, Y., & Noack, B. R. (2020). Optimization and sensitivity analysis of active drag reduction of a square-back Ahmed body using machine learning control. *Physics of Fluids*, *32*(12), 125117. https://doi.org/10.1063/5.0033156

Feller, H. G., & Kharrazi, Y. (1984). Cavitation erosion of metals and alloys. *Wear*, *93*(3), 249-260. https://doi.org/10.1016/0043-1648(84)90199-6.

Forder, A., Thew, M., & Harrison, D. (1998). A numerical investigation of solid particle erosion experienced within oilfield control valves. *Wear*, *216*(2), 184-193. https://doi.org/10.1016/S0043-1648(97)00217-2

Fuyan, L., & Hesheng, S. (1991). The effect of impingement angle on slurry erosion. *Wear*, *141*(2), 279-289. https://doi.org/10.1016/0043-1648(91)90274-X

Gomez-Flores, A., Heyes, G. W., Ilyas, S., & Kim, H. (2022). Effects of artificial impeller blade wear on bubble–particle interactions using CFD (k–ε and LES), PIV, and 3D printing. *Minerals Engineering*, *186*, 107766. https://doi.org/10.1016/j.mineng.2022.107766.

Hattori, S., & Kishimoto, M. (2008). Prediction of cavitation erosion on stainless steel components in centrifugal pumps. *Wear*, *265*(11-12), 1870-1874. https://doi.org/10.1016/j.wear.2008.04.045.

Huang, S., Huang, J., Guo, J., & Mo, Y. (2019). Study on wear properties of the flow parts in a centrifugal pump based on EDEM–fluent coupling. *Processes*, *7*(7), 431. https://doi.org/10.3390/pr7070431.

Mao, L., Gan, L., Li, W., & Zhang, P. (2022). Failure analysis on weld joint of centrifugal pump diffuser for oil and gas pipeline transportation. *Engineering Failure Analysis*, *140*, 106620. https://doi.org/10.1016/j.engfailanal.2022.106620.

Moghimi, P., & Rafee, R. (2018). Numerical and experimental investigations on aerodynamic behavior of the Ahmed body model with different diffuser angles. *Journal of Applied Fluid Mechanics*, *11*(4), 1101-1113. https://doi.org/10.29252/JAFM.11.04.27923.

Mortazavi, F., Riasi, A., & Nourbakhsh, A. (2017). Numerical investigation of back vane design and its impact on pump performance. *Journal of Fluids Engineering*, *139*(12), 121104. https://doi.org/10.1115/1.4037281

Padhy, M. K., & Saini, R. P. (2011). Study of silt erosion on performance of a Pelton turbine. *Energy*, *36*(1), 141-147. https://doi.org/10.1016/j.energy.2010.10.060

Pagalthivarthi, K. V., Gupta, P. K., Tyagi, V., & Ravi, M. R. (2011). CFD prediction of erosion wear in centrifugal slurry pumps for dilute slurry flows. *The Journal of Computational Multiphase Flows*, *3*(4), 225-245. https://doi.org/10.1260/1757-482X.3.4.225.

Peng, G., Huang, X., Zhou, L., Zhou, G., & Zhou, H. (2020). Solid-liquid two-phase flow and wear analysis in a large-scale centrifugal slurry pump. *Engineering Failure Analysis*, *114*, 104602. https://doi.org/10.1016/j.engfailanal.2020.104602.

Pirouzpanah, S., Patil, A., Chen, Y., & Morrison, G. (2019). Predictive erosion model for mixed flow centrifugal pump. *Journal of Energy Resources Technology*, *141*(9), 092001. https://doi.org/10.1115/1.4043135.

Rajani, B. N., Kandasamy, A., & Majumdar, S. (2012). On the reliability of eddy viscosity based turbulence models in predicting turbulent flow past a circular cylinder using URANS approach. *Journal of Applied Fluid Mechanics, 5*. http://doi.org/10.36884/jafm.5.01.11959

Ren, K., Chen, Y., Gao, C., & Zhang, W. (2020). Adaptive control of transonic buffet flows over an airfoil. *Physics of Fluids*, *32*(9), 096106. https://doi.org/10.1063/5.0020496

Shah, S. N., & Jain, S. (2008). Coiled tubing erosion during hydraulic fracturing slurry flow. *Wear*, *264*(3-4), 279-290. https://doi.org/10.1016/j.wear.2007.03.016.

Sharma, S., & Gandhi, B. K. (2022). Experimental investigation on rotating domain wear of hydrodynamic machine due to particulate flow. *Powder Technology*, *410*, 117884. https://doi.org/10.1016/J.POWTEC.2022.117884.

Song, X., Yao, R., Shen, Y., Bi, H., Zhang, Y., Du, L., & Wang, Z. (2021). Numerical prediction of erosion based on the solid-liquid two-phase flow in a double-suction centrifugal pump. *Journal of Marine Science and Engineering*, *9*(8), 836. https://doi.org/10.3390/JMSE9080836.

Tarodiya, R., & Gandhi, B. K. (2017). Hydraulic performance and erosive wear of centrifugal slurry pumps-A review. *Powder Technology*, *305*, 27-38. https://doi.org/10.1016/j.powtec.2016.09.048

Walker, C. I., & Robbie, P. (2013). Comparison of some laboratory wear tests and field wear in slurry pumps. *Wear*, *302*(1-2), 1026-1034. https://doi.org/10.1016/j.wear.2012.11.053.

Wang, Y., He, T., Ding, Q., Gao, P., Tao, R., & Zhu, Z. (2022a). Analysis of internal flow and wear characteristics of binary mixture particles in centrifugal pump based on CFD-DEM. *Processes*, *10*(4), 681. https://doi.org/10.3390/PR10040681.

Wang, Y., Wang, X., Chen, J., Li, G., Liu, H., & Xiong, W. (2022b). An experimental insight into dynamic characteristics and wear of centrifugal pump handling multi-size particulate slurry. *Engineering Failure Analysis*, *138*, 106303. https://doi.org/10.1016/J.ENGFAILANAL.2022.106303.

Zhang, J., Kang, J., Fan, J., & Gao, J. (2016). Study on erosion wear of fracturing pipeline under the action of multiphase flow in oil & gas industry. *Journal of Natural Gas Science and Engineering*, *32*, 334-346. https://doi.org/10.1080/02726351.2010.523926.

Zhou, L., Wang, W., Hang, J., Shi, W., Yan, H., & Zhu, Y. (2020). Numerical investigation of a high-speed electrical submersible pump with different end clearances. *Water*, *12*(4), 1116. https://doi.org/10.3390/w12041116